Numerical simulations of pore isolation and competition in idealized micro-spall process

Wojciech Aniszewski[a,*], Stéphane Zaleski[a], Antoine Llor[b], Leon Malan[c]

[a] *Sorbonne Université, CNRS, Institut Jean le Rond d'Alembert, 75005 Paris, France*
[b] *CEA, DAM, DIF, 91297 Arpajon Cedex, France*
[c] *University of Cape Town, Cape Town 7701, South Africa*

Abstract

The 'micro-spall' phenomenon is a variant of fragmentation process—or spall fracture—that is traditionally discussed in context of solid materials (metals). However it concerns situations in which the medium is fully or partially *melted*—be it due to kinetic impact, detonation or laser loading. The phenomenon takes place at sub-micrometer and sub-microsecond scales making it inaccessible to direct experimental observation; so far, investigations have been restricted to observations of late time "post-mortem" fragments.

In this context, it becomes a viable approach to apply analysis using numerical description for fluids. This work presents such an application for an idealized rapid uniaxial (one-dimensional) system expansion. Cavitation in the medium is represented by including vacuous pores or cavities with surface tension whose growth and interaction are traced in time. The simulations reveal two main regimes of pore growth regulated by a characteristic Weber number.

Keywords: micro spall, cavity, Volume of Fluid (VOF), free surface, pore competition

1. Introduction

Cavitation and micro-spall (see for instance Signor et al., 2010, and references therein) appear when a weakly compressible (or expansible) liquid is suddenly submitted to a large volume growth (expansion) resulting in negative pressures. This process, which appears in many practical applications of interest, occurs when an initially solid medium is subject to an unsustained impact or detonation and is entirely or partly melted in the process. Once the system starts expanding, the pressure drop causes the onset of cavitation with pores (or bubbles filled with vapor) appear. After the initial phases of uniform expansion and pore opening, a longer-lasting phase of pore growth and competition appears, which is especially difficult to investigate either experimentally or numerically (de Rességuier et al., 2010; Signor et al., 2010).

We present here numerical simulations of this latter phase for idealized conditions relevant to micro-spall. This paper picks up on a previously published study of Malan et al. (2018) which presented low-Weber number expansions of the system (with constant expansion rates). Malan et al. (2018) focused on a *competition* phenomenon in which expansion of some of the pores caused their neighboring pores to collapse: in other words, there was a volume transfer between the pores without actual contact and merger between them. The pore competition effect is important as it is the main phenomenon driving the evolution in time of the statistical distribution of pore sizes (Everitt et al., 2006). Small pores shrink and eventually disappear as their volume is transferred to large pores. Pore statistics and pressure evolution profiles can then be obtained for future modeling purposes. Hypothetically, continued competition accompanied by coalescence could lead to formation of larger pores—or even of a single pore in the case of a spatially limited system. In this work, we focus on the practically relevant case of constant speed expansions whose rate decrease with time: the corresponding Weber numbers typically start and end respectively at ranges above and below the competition threshold.

Thus, our idealized assumptions are incompressible inviscid fluid, vanishing vapor pressure in cavities, homogeneous uniaxial "ballistic" expansion, perturbed face-centered-cubic lattice arrangement of pores. Under these assumptions, the system is characterized by a single dimensionless group, the Weber number based on the number of pores per unit volume. The "ballistic" expansion signifies evolution in which We rapidly decays: in the initial stages of expansion the flow is entirely dominated by inertia and the pores expand as if they were isolated (Ilinskii et al., 2007). As We drops the system transitions into a regime in which the bubbles interact and capillary pressure becomes significant. We investigate this transition in more detail below. Results indicate that both the uniform growth in the initial expansion phase, as the later "competition" (Everitt et al., 2006) regime can be captured.

2. Elementary characterization of ideal micro-spall

2.1. Mean expansion field

We investigate a fluid element undergoing expansion following a shock and release history. As sketched in the volume and

*Corresponding author. Tel: +33 1 44 27 87 14.
Email addresses: aniszewski@dalembert.upmc.fr (Wojciech Aniszewski), antoine.llor@cea.fr (Antoine Llor)
URL: http://www.lmm.jussieu.fr/~zaleski/index.html (Stéphane Zaleski)

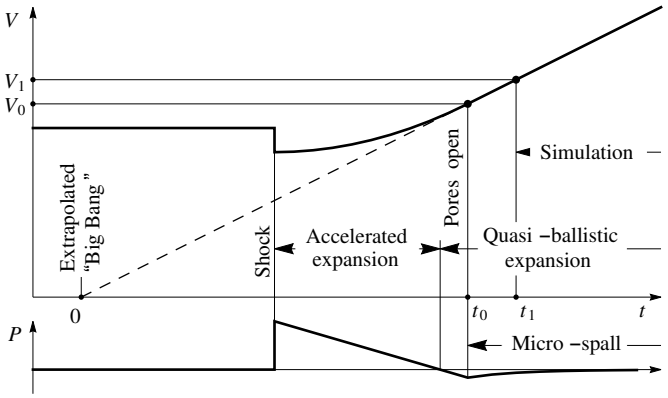

Figure 1: Sketched evolution of mean macroscopic volume and pressure of a material element undergoing mico-spall. As qualitatively represented, the initial pressure produced by the shock and the final spall stress are here assumed respectively large and small enough that the eventual expansion is nearly ballistic. This ballistic evolution can then be backward extrapolated to vanishing volume which defines the (arbitrary) time origin. As indicated, the system evolution is here simulated after pores have opened and local fluid density has returned to a nearly uniform and constant value.

pressure profiles of Fig. 1, pressure drops due to the accelerated expansion and eventually becomes negative. At one point the cohesive limit of the fluid is reached and pores open: in this micro-spall phase, surface tension around the pores produces a macroscopic negative stress. If this spall stress is weak enough compared to the stored momentum the system eventually evolves in a quasi-ballistic way. The micro-spall phenomenon can appear regardless of the structure of the strain tensor—which in general displays three different eigenvalues—but we shall focus here on the most common situation of uniaxial expansion and more marginally on the theoretically useful situation of isotropic expansion.

For a small enough material volume, the average strain can be considered as uniform and the backward-extrapolated positions of all the fluid elements collapse to a single point: this is the virtual "Big Bang" that provides the time and space origins in all the following, $t = 0$ and $\mathbf{x} = \mathbf{0}$. Depending on the strain dimension and depending on the selected coordinate system, Lagrangian $\mathbf{X}$ or Eulerian $\mathbf{x}$, the mean velocity field in the material volume can always be written as

	Lagrangian	Eulerian	
Uniaxial	$\overline{u}(X,t) = \overline{u}(X,t_0) = X/t_0,$	$\overline{u}(x,t) = x/t,$	(1a)
Isotropic	$\overline{\mathbf{u}}(\mathbf{X},t) = \overline{\mathbf{u}}(\mathbf{X},t_0) = \mathbf{X}/t_0,$	$\overline{\mathbf{u}}(\mathbf{x},t) = \mathbf{x}/t,$	(1b)

where the Lagrangian coordinate $\mathbf{X}$ is the actual position at reference time t_0, and x and X represent the first coordinates of the $\mathbf{x}$ and $\mathbf{X}$ position vectors. Equations (1) describe *expansion*, as the "Hubble time" t_0 is assumed positive. The uniform but non-constant divergence of the mean velocity field is

$$\boldsymbol{\nabla} \cdot \overline{\mathbf{u}} = d/t, \tag{2}$$

where dimensionality d is 1 or 3 for respectively uniaxial or isotropic expansions, and is related to mean density through

$$\frac{\mathrm{d}}{\mathrm{d}\,t} \ln \overline{\rho} = -\boldsymbol{\nabla} \cdot \overline{\mathbf{u}}. \tag{3}$$

Combining (2) and (3) yields

$$\overline{\rho} = \overline{\rho}_0 \, (t_0/t)^d, \tag{4}$$

where the reference state is conveniently taken here at time $t = t_0$ where cavitation nuclei appear (Batchelor, 1967) (and pores open) and where the mean density coincides with the fluid density $\overline{\rho}_0 = \rho_l$.

Equations (1) are solutions of the Euler equation

$$\partial_t \overline{\mathbf{u}} + (\overline{\mathbf{u}} \cdot \boldsymbol{\nabla}) \overline{\mathbf{u}} = -\frac{1}{\overline{\rho}} \boldsymbol{\nabla} \overline{p}, \tag{5}$$

with zero mean pressure gradient and uniform but non-constant mean density $\overline{\rho}$. The ultimate goal of modeling is to provide a closure relationship between $\overline{\rho}$, $\overline{\mathbf{u}}$, and $\overline{p}$ so as to simulated the effect of micro-spall on large scale dynamics (possibly elliptic unstable).

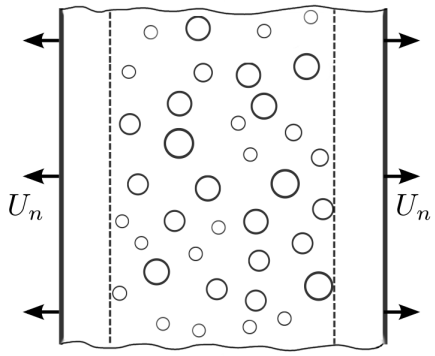

Figure 2: Schematic representation of idealized micro-spall as a pore cluster undergoing expansion along the x direction.

2.2. *Mean pore characteristics*

At microscopic scales, micro-spall displays fluctuations on all its smooth large-scale fields. As sketched in Fig. 2, a first approximation convenient to capture surface tension effects consists in assuming all pores as spherical, with no internal mass and pressure (vanishing vapor pressure), and furthermore with identical radii $R(t)$ and no translation velocity with respect to their surroundings (Caflisch et al., 1985). Therefore, no coalescence effects can be present, and the number of pores is constant and equal to the number of cavitation nuclei at $t = t_0$. The mean number density of pores N then scales as mass density (4)

$$N = N_0 \, (\overline{\rho}/\rho_l) = N_0 \, (t_0/t)^d. \tag{6}$$

In a more realistic situation were pores may collapse or merge, as in the present simulations, this relationship does not hold.

Under the simplifying assumption of local spherical symmetry the number density of pores provides their geometric characteristics. Each pore influences a mean spherical volume defined

by the Wigner–Seitz radius $\ell(t)$ (Girifalco, 2000):

$$\frac{4\pi}{3}\ell^3 N = 1. \tag{7}$$

As the mean volume fraction of liquid is $(\overline{\rho}/\rho_l)$, identification of volume fractions in the Wigner–Seitz sphere yields the mean pore radius $R(t)$ from the equivalent relationships

$$\frac{4\pi}{3}R^3 N = 1 - (\overline{\rho}/\rho_l) = 1 - (t_0/t)^d, \tag{8a}$$

$$\frac{4\pi}{3}R^3 N_0 = (\rho_l/\overline{\rho}) - 1 = (t/t_0)^d - 1. \tag{8b}$$

Combining (8) and (7) yields the aspect ratio of the equivalent mean spherical shell

$$(R/\ell)^3 = 1 - (\overline{\rho}/\rho_l) = 1 - (t_0/t)^d. \tag{9}$$

Equations (8) to (9) hold even if, due to collapse and merger, (6) may not.

2.3. Kinetic and surface energies, Weber number

Under expansion, the kinetic and surface energies evolve and the overall behavior of the system is characterized by their ratio: the Weber number. Because the fluid is assumed incompressible and inviscid, these two energies fully control the system and only two regimes are expected: all situations can be collapsed according to the Weber number alone. The energies can be estimated within the framework of the mean spherical pore of Section 2.2.

The surface energy of a single mean pore is given by the surface tension coefficient σ

$$E_s = 4\pi R^2 \sigma. \tag{10}$$

The kinetic energy is obtained by assuming the velocity field to be radial and divergence free around the mean pore, with a vanishing mass flux at the Wigner–Seitz boundary

$$E_k = \int_R^\ell \tfrac{1}{2}\rho_l \mathring{\ell}^2 \left(\frac{\ell}{r}\right)^4 4\pi r^2 \,\mathrm{d}\, r = 2\pi\rho_l \left(\frac{d/3}{t}\right)^2 \ell^6 \left(\frac{1}{R} - \frac{1}{\ell}\right), \tag{11}$$

where $\mathring{\ell}$ is the time derivative of ℓ which according to (7) and (6) verifies $\mathring{\ell}/\ell = (d/3)/t$. Using identities (6) to (9) we can now represent both mean radius R and Wigner-Seitz radius ℓ only in terms of t and state of the system at t_0. Namely, from (6) we have

$$N_0 \left(\frac{t_0}{t}\right)^d = \frac{3}{4\pi\ell^3}, \tag{12}$$

thus ℓ can be expressed as:

$$l = \sqrt[3]{\frac{3}{4\pi N_0 \left(\frac{t_0}{t}\right)^d}}. \tag{13}$$

Using the aspect ratio (8) we find that

$$R = \ell\sqrt[3]{1 - \left(\frac{t_0}{t}\right)^d}. \tag{14}$$

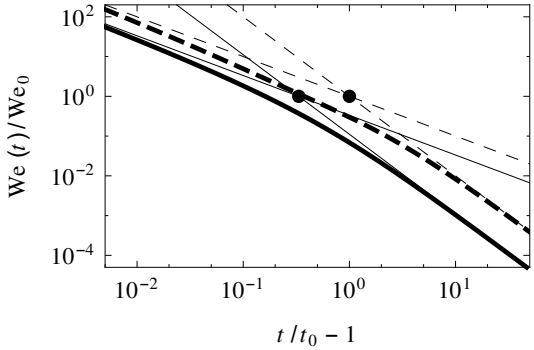

Figure 3: Evolution of the reduced Weber number of the characteristic mean pore during expansion We(t)/We$_0$ in (15a) as a function of reduced time $t/t_0 - 1$ (log scales); solid lines: uniaxial expansion; dashed lines: isotropic expansion; thin lines: asymptotic limits with slopes -1 and -2. Points represent transitions between asymptotic behaviors at small and large times where We/We$_0 = 1$.

Subsequently, we substitute both (13) and (14) in (11), so the Weber number We $= E_k/E_s$ is eventually obtained as

$$\mathrm{We}(t) = \mathrm{We}_0 \,\frac{d^2\,(t_0/t)^{2-d}}{3\,(1-(t_0/t)^d)}\left(1 - \sqrt[3]{1-(t_0/t)^d}\right), \tag{15a}$$

$$\mathrm{We}_0 = \frac{\rho_l}{8\pi\sigma N_0 t_0^2}. \tag{15b}$$

Notice here that the Weber scaling We$_0$ built from quantities at $t = t_0$ is *not* equal to We(t_0): it is actually found that We$(t) =$ We$_0$ at $t/t_0 \approx 1.16$ and 1.38 for respectively $d = 1$ and 3—with volume expansion ratios of $\rho_l/\overline{\rho} = (t/t_0)^d \approx 1.16$ and 2.60. As illustrated in Fig. 3, the Weber number We(t) diverges as $(t - t_0)^{-1}$ for $t \to t_0$ and vanishes as $(t - t_0)^{-2}$ for $t \to \infty$. The expressions in (15) were scaled in such a way that these asymptotes actually intersect at We$_0$ for either $t/t_0 = 4/3$ or 2 for uniaxial and isotropic expansions as shown in Fig. 3.

The fact that the Weber number We(t) decreases from virtually unbounded values down to zero shows that two regimes should appear during expansion. At early times, kinetic energy dominates and expansion is quasi-ballistic, whereas at late times, surface tension dominates, thus slowing expansion and inducing pore interactions through Laplace pressure. The transition will appear more or less early depending on the initial conditions defined by the Weber scaling We$_0$ and possibly in either of the $t \to t_0$ or $(t - t_0)^{-2}$ regimes represented in Fig. 3. According to the N_0 dependence in (15b), these two regimes correspond to respectively dense or sparse distributions of cavitation nuclei.

2.4. Pressure Evolution

Mean macroscopic p evolution has been sketched in Figure 1, presenting its sharp drop after the shock and during accelerated expansion phase. At the moment of pore opening pressure chanes sign, while its growth is restored in the micro-spall regime. We can trace this evolution in a more detailed manner using velocity potential $\phi(t)$ and mean radii R. We first formulate the Bernoulli equation

$$\phi_t + \frac{u^2}{2} + \frac{p - p_\infty}{\rho} = 0, \tag{16}$$

where $u = \dot{R}R^2/r^2$ and thus $\phi = -\dot{R}R^2/r$. This leads to a Rayleigh-Plesset type expression for pressure "at infinity"

$$p_\infty = \rho_l \left(\ddot{R}R + \frac{3}{2}\dot{R}^2 \right) - \frac{2\sigma}{R}. \tag{17}$$

Having discussed the mean spherical cell aspect ratio in the previous subsection, we can now solve for $\ddot{R}$ using (8) leading to

$$\ddot{R} = -\frac{2l_0}{9\sqrt[3]{t}} (t - t_0)^{-5/3}, \tag{18}$$

which allows us to retrieve p_∞ by substituting back to (17):

$$p_\infty(t) = \frac{\rho_l l_0^2}{18\sqrt[3]{t_0^2 (t - t_0)^4}} - \frac{2\sigma}{\rho_l} \sqrt[3]{\frac{t_0}{t - t_0}}. \tag{19}$$

It is easy to verify that the above formula depicts a curve whose shape corresponds closely to the pressure curve sketched in Figure 1 as long as $t_0 \ll l_0/$ which is normally the case, as mean Wigner-Seitz radii will be significant at the moment of pore opening.

While the simulations described in this work are set up in such a way that initial time value is $t_1 > t_0$, it is interesting to study the effect of the propagating pressure pulse on the system. This reasoning is not without substance, as in computational practice the flow will respond to imposed expansion boundary conditions used here with a negative pressure pulse (see e.g. Figure 7 in (Malan et al., 2018) and results presented in Section 5). We assume incompressibility, however because of the negative pressure created by surface tension on the bubbles/pores, the system could be seen as having negative compressibility, so that the speed of sound c, given below:

$$c^2 = \frac{\partial p}{\partial \rho} \tag{20}$$

is imaginary. Taking this into account, and linearizing the Euler equation (5) and the mass conservation equation (3) we obtain

$$|c|^2 \partial_{xx}^2 p + \partial_{tt}^2 p = 0 \tag{21}$$

A quick estimate based on Laplace's law leads to

$$|c|^2 = \frac{\sigma}{4\pi N \rho_l R^4}. \tag{22}$$

A conclusion that may be drawn from the pressure equation (21) is that as soon as the pressure has been affected by growing pores in a region, the pressure pulse will propagate to the rest of the system at a speed $|c|$. Such a propagating solution, of the form $p = \mathrm{atan}(x/|c|t)$, is possible even in the elliptic system case. The speed $|c|$ of the wave may be comparable to the initial speed $L_0/(2t_1)$ of the expansion wave; comparison will be dependent on surface tension and Weber number.

3. Computational Methods

3.1. The Paris Simulator

The simulations presented in this paper use the Parallel Robust Interface Simulator (or PaRIS, PariSimulator Ling et al., 2015; Malan et al., 2018), which is a is an in-home CFD code developed jointly at Institute ∂'Alembert, University of Notre-Dame and University of Bologna. Paris is a classical, MAC-type solver using uniform, cuboidal meshes. Its strengths lie in a very efficient MPI parallelisation and broad variety of implemented computational methods, especially for interfacial, two-phase flows. These include e.g. Front Tracking (Tryggvason et al., 2011), Volume of Fluid (Hirth and Nichols, 1981) and tracking Lagrangian particles. The code is GPL licensed[1] and publicly available[2].

A well known projection scheme (Tryggvason et al., 2011) is used to solve momentum conservation equations. We will explain it briefly by showing a way the algorithm progresses from n-th to $n+1$-st step. Knowing the values of all fields at the end of $n-$th step, we are starting with the definition of the temporary velocity field $\mathbf{u}^*$

$$\frac{\mathbf{u}^* - \mathbf{u}^n}{\Delta t} = -\mathbf{u}^n \cdot \boldsymbol{\nabla}_h \mathbf{u}^n, \tag{23}$$

which can be found easily since, at the end of n-th time-step it is the only unknown in above formula. Symbol $\boldsymbol{\nabla}_h$ stands for the discrete differential operator. This is a *projection* step since velocity is projected onto a space with zero pressure field. We can now write a discrete version of (5) which involves $\mathbf{u}^*$, only this time changing the way the approximation of temporal derivative is formulated

$$\frac{\mathbf{u}^{n+1} - \mathbf{u}^*}{\Delta t} = -\frac{\boldsymbol{\nabla}_h p^{n+1} + \sigma\kappa\mathbf{n}\delta_s}{\rho^n}, \tag{24}$$

where superscript $n+1$ stands for the value at the end of n-th time-step. Notice surface tension contribution has been included in (24): σ stands for the surface tension coefficient, $\mathbf{n}$ is the vector normal to the interface, while κ is scalar curvature—also the restriction to the interfacial surface S is ensured by the δ_S operator. If now we apply a divergence operator to both sides of (24) and remember that we assume $\boldsymbol{\nabla} \cdot \mathbf{u}^{n+1}$ to vanish, we obtain the Poisson equation from which pressure p^{n+1} can be found

$$\boldsymbol{\nabla}_h \cdot \left[\frac{\Delta t}{\rho^n} \boldsymbol{\nabla}_h p^{n+1} \right] = \boldsymbol{\nabla}_h \cdot \mathbf{u}^* + \boldsymbol{\nabla}_h \cdot \left(\frac{\Delta t}{\rho^n} \sigma\kappa\mathbf{n}\delta_s \right). \tag{25}$$

In most computational codes numerical solution of (25) is the stage to which most computational cost (up to 90 percent) is associated; especially in multi-phase flows with variable density. Once (25) is solved with p^{n+1} found, both it and $\mathbf{u}^*$ are used to find the divergence-free velocity at the end of the time-step

$$\mathbf{u}^{n+1} = \mathbf{u}^* - \frac{\Delta t}{\rho_n} \left(\boldsymbol{\nabla}_h p^{n+1} + \sigma\kappa\mathbf{n}\delta_s \right) \tag{26}$$

thus ending the procedure. Many authors call (26) a "correction" step as solenoidal character of $\mathbf{u}^{n+1}$ is ensured thereby.

[1] https://www.gnu.org/licenses/gpl.html

[2] Available at http://www.lmm.jussieu.fr/~zaleski/paris/index.html

3.2. Interface Tracking

As mentioned, normal vectors $\mathbf{n}$ and curvatures κ in above equations[3] are found from the color/fraction function C, whose advection equation follows in discrete form

$$\frac{C^{n+1} - C_n}{\Delta t} + \boldsymbol{\nabla}_h \cdot (C\mathbf{u}^n) = 0. \tag{27}$$

Above equation cannot be solved directly, as C is a sharp jump function: the jump would be diffused by numerical errors (Youngs, 1984). Therefore, in most applications (27) is solved using specially crafted geometrical reconstruction–advection schemes such as CIAM (Li, 1995) or PLIC (Aniszewski et al., 2014). Normal vectors and curvature are calculated using Height Functions technique (Cummins et al., 2004; Popinet, 2003) which has multiple provisions for the cases of insufficient grid resolutions and/or specific interface configurations.

3.3. Free Surface Solver

To implement the boundary conditions on the interface, a free surface method has been implemented in PariSimulator (Malan and Zaleski, 2015). The flow within the pores is not explicitly solved for (except up to two interior cell layers as explained below), additionally in this paper we initially set the p_p pressure value to zero. With that assumption the flow is in fact a quasi-single phase flow, but surface tension is accounted for on the pore surfaces. Still, pressure p_p inside the pores is defined, although it is assumed spatially constant inside them and is calculated using the polytropic equation of state (Malan et al., 2018).

1. The pressure field is extrapolated onto the interface which is necessary for (25). The boundary value of the gradient is computed as
$$p^* = p_p - \sigma\kappa, \tag{28}$$
where p_p is constant pore pressure, and $\sigma\kappa$ is Laplace pressure, thereby assuring that surface tension effect is accounted for. The p^* value is used for $\boldsymbol{\nabla}_h$ operators in cells neighboring the interface;
2. The velocity field is extrapolated to within the pores; these values are necessary for higher-order gradient operators for cells neighboring the interface. Extrapolation is based on liquid velocity, which is extended to two grid-cell layers (or 'levels') within pore/bubble interior by geometrical fitting and least-squares minimization;
3. Finally, the extrapolated velocities in level 1 and 2 cells are corrected to ensure the new field is divergence free.

Computational tests have shown the above procedure amounts to approximately 10% of CPU cost in a massively parallel simulation compared with Poisson solver cost standing at 80%.

Limitation introduced by current implementation of the above algorithm is—apart from aforementioned necessity of pre-seeding the pores—that the pores cannot coalesce, as it is not yet made compatible with the point 2. of the above list, as topology change of the pores cannot be accounted for. The model however allows for the pore collapse, to which the system responds with a pressure pulse. It is also interesting to notice that the pores can undergo displacement (i.e. move) for example due to non-balanced surface tension force distributions. More details on the Free Surface sub-solver implementation can be found in Malan et al. (2018).

3.4. Implementation

In implementation, we apply the Hypre package's (Falgout and Yang, 2002) SMG (semi-coarsening multigrid solver with 3D plane smoothing) for numerical solution of the Poisson problems (25) on the structured, cubic meshes that PariSimulator uses. Advection terms in (23) are calculated using central differencing with WENO (Shu, 1997) and Superbee-type (Sweby, 1984) slope limiters. Interface curvatures for (24) are calculated with a combination of techniques providing for various stencil shapes and built within the framework of Height Function method (Cummins et al., 2004) and with the mixed-Youngs-central (Youngs, 1984) scheme for normal vector $\mathbf{n}$ computation. Finally, Volume of Fluid method is used to track the interface, using explicit geometric reconstruction of the interface (Scardovelli and Zaleski, 2000) and CIAM/PLIC (Aniszewski et al., 2014) scheme to compute fluxes $c\mathbf{u}^n$ in (27). A cavity tagging and Lagrangian particle-tracking algorithm (Ling et al., 2015) are used to retrieve statistics of cavity sizes.

The method was validated comparing numerical solutions to solutions of the Rayleigh–Plesset equation for oscillating bubbles (Malan and Zaleski, 2015; Malan et al., 2018).

4. Simulation setup

4.1. Initial Conditions

To simulate the idealized micro-spall phenomena in a way specified in Section 2 we have set up the simulations in a following way. Cubical computational domain is used (see Fig. 2), containing a given number of pre-seeded pores in a FCC (Face-Centered Cubic) lattice. The domain is expanded in x direction as assumed in Section 2. More specifically, the proper temporal evolution of the velocity field described by (1) is ensured by initializing:

- the x-velocity component to $u = x$ with proper translation and scaling, so that for $t = t_1$ we have $u(0, t_1) = -u_n$, $u(L/2, t_1) = 0$ and $u(L, t_1) = u_n$ where u_n is the outflow velocity;
- the outflow boundary condition for the velocity field $\mathbf{u} = (u, v, w)$ in such manner, that
$$u_n = 1/t_1, \tag{29}$$
where $t_1 > 0$; for subsequent moments of simulated time t (29) is held so that $|u_n(t)| = 1/t$ at all times;
- the v and w components to zero.

[3] The same applies for the approximation of Dirac delta δ_s.

This implies usage of Dirichlet boundary condition for u in the x direction, which is time-dependent as said above. Neumann boundary condition for p is thus applied on the $x+$ and $x-$ walls. Imposing Dirichlet boundary conditions for pressure (instead of velocity) could be a valid choice for this type of flow, however—unlike the cases in which pores are wholly contained in the domain (Malan et al., 2018)—uniaxial expansions discussed here involve pores crossing outer domains along x axis. This in turn would make Dirichlet condition for pressure inconsistent.

Periodic boundary conditions are imposed on YZ walls. For the condition to be compatible with the pore cluster geometry, it is re-shaped by adjusting the pore-free buffer surrounding it. More precisely, due to periodic condition in YZ directions, the buffer is present only in the x direction (visible as empty region in Fig. 2), i.e. for $x < 0.12$ and $x > 0.88$ the domain contains no pores at $t = t_1$. Cubic domain of size $L = 1$ is assumed with initially 365 pores. Thus, we arrive at value of $\ell \approx 0.14$.

4.2. Physical parameters and computational grids

We describe simulation results concerning the uniaxial expansion using example simulations whose parameters are given in Table 1.

Consider now the simulation domain $(-L_0/2, L_0/2)^3$ within which spherical pores are initialized with non-zero radii (which is necessary due to limitations of Paris code) i.e. numerical simulations are started at $t_1 > t_0$. With this in mind, the mean radii distribution right after pore opening is

$$R(t_1) = L_0 \left[\frac{3}{4\pi N_0} \left(\frac{t_1}{t_0} - 1 \right) \right]^{1/3}, \tag{30}$$

which is how pores are defined as a initial simulation condition. In this computational configuration, it is desirable for $R(t_1)$ to be possibly small, to offer a large range of scales - in other words, headroom for $V(t)$ growth before the pores coalesce. A favourable relation would be

$$\Delta x \ll R(t_1) \ll \ell \ll L_0. \tag{31}$$

where Δx is the grid size. The leftmost and rightmost inequalities of (31) are however slightly relaxed for the results presented in this paper due to grid resolutions used, as will be detailed below.

Example simulations have been performed using 256^3 grid points. For the first simulation ("I"), value of Weber number (15a) at t_1 is 512.83. The pore lattice is configured as specified above, with liquid characteristics found in Table 1. In the Table, "I" and "C" are labels designating the "Isolation" and "Competition" regimes; We and Ma are dimensionless Weber and Mach numbers, ρ and σ are respectively liquid density and surface tension applied at the pore surfaces, while var(r) stands for the a variation in pore radii applied to the initial condition. Mach number values presented in Table 1 are calculated using the speed of sound c as defined by (22).

As mentioned above (see (30)), due to the applied spatial resolution, certain restrictions on the initial pore radii $R(t_1)$ are imposed, as the pores must be properly represented by the interface tracking method at t_1 . This representation requires e.g. that gradients of the fraction function C can be resolved near the interface (to calculate interface normals) with finite difference operators. Having the size of domain L_0 and initial pore number N_0 fixed, and imposing additional restriction $R > 3\Delta x$ we e.g. choose $t_1 = 0.08$ for the presented simulation of isolation regime (see Table 1). This amounts to $R(t_1)/\Delta x \approx 3.44$ which is considered resolved (Tryggvason et al., 2011) in that proper values of curvature can be computed for pores of that radius[4]. Due to the dependence (8) between simulation initial time t_1 and bubble/pore radii, any decrease of t_0, and t_1/t_0 would reduce R, which in turn would imply an increased grid resolution.

5. Results

5.1. Isolation regime

Figure 4a presents cluster geometry at $t' = t_1 + 1.929 \cdot 10^{-2}$. Uniform expansion of the bubbles/pores is clearly visible with pore layers closest to the walls along the x axis visibly elongated due to the fact that convection is strongest there. At $t \geq t_1 + 1.92 \cdot 10^{-2}$ one observes pore radii of order of ℓ. Nearly all pores are ellipsoidal in shape, and have expanded beyond the region of the simulated volume, including periodic yz walls. Moreover, the outer layer of pores has now completely disappeared (have been convected out) from the simulation domain, as only remnant interfacial cells are visible.

Temporal evolution of the pore volume fraction V_g for "I" regime flow is seen in Fig. 5. Seeing as all volume change in the liquid results from growth of the pores, we can supplement (4) by a following expression for pore volumes:

$$V_g = L_0^3 (1 - \frac{t_0}{t}). \tag{32}$$

Thus calculated pore volume fraction $V_g(t_1 = 0.08)$ should be $3.59 \cdot 10^{-3}$, however it is visibly lower in simulation, due to the initial variance in pore radii (Table 1) introducing additional volume. Proper scaling has thus been used for the analytic formula to make up for that. Another source of a difference between (32) and simulated pore value is –as mentioned in context of Fig. 4a – that the pores leave the computational domain as it is expanded, which in the "I" simulation takes place at $t + t_1 > 0.05$.

For the isolation regime simulation, we additionally present in Fig. 6 the profiles for $\langle p \rangle$ (Fig. 6a) and $\langle u_x \rangle$ (Fig. 6b) measured along the x axis. These are taken from the early simulation stage ($t = 6.732 \cdot 10^{-3}$) and confirm that the evolution of the system is indeed in the ballistic regime, as velocity profile conforms to a linear as predicted in (1). The 'wavy' character of the plot if Fig. 6b is caused by inclusion of zero velocities (inside the pores) to the average. Similarly, we observe no variance in $\langle p \rangle$ (Fig. 6a) when focusing our attention on the lattice-occupied part: for $x < 0.12$ and $x > 0.88$ there is an empty "buffer zone" in the x direction as mentioned above.

[4] Not accounting for about 5 percent variance in R in initialization.

Table 1: Parameters for two examples of simulations of the uniaxial expansion, as explained in text.

Label	ρ	σ	t_1	t_0	var (r)	We(t_1)	Ma(t_1)
I	1000	0.1	$8 \cdot 10^{-2}$	$7.797 \cdot 10^{-2}$	50%	512.83	15
C	444	1	2.1	2.092	50%	$3.3 \cdot 10^{-2}$	0.12

5.2. *Competition regime*

We continue the description of the results with the second simulation ("C") which, as seen in Table 1 is characterized by a much lower Weber number. As a result of this, the evolution of the pore lattice is no more dominated by expansion and the pores are not isolated, and the elongated shapes of the pores visible in Fig. 4a give way to a "pore competition" phenomenon (Everitt et al., 2006). As visible in Fig. 4b, number of pores has either shrunk or is at the verge of imploding, their volume being overtaken by a group of large pores. Distribution of radii in the latter group is rather isotropic with all pores roughly spherical, while ellipsoidal forms are absent. For situation presented in Fig. 4b average pressure $\langle p \rangle$ has a negative value. This is due to the fact that positive pressure field is associated with expanding liquid, while for low Weber number negative Laplace pressures (capillary force) dominate the pressure distribution. We will revisit this subject in Fig. 9.

Both increased radii variation and implosion events are visible in Fig. 7 which displays individual pore volume histories for the larger (brown lines) and smaller (blue lines) Weber numbers. To the accuracy allowed by post-processing software, each line displays volume of an individual pore, with about 300 pores tracked for each simulation. Time is normalized by capillary timescale (Malan et al., 2018)

$$\tau_R = \left(\frac{\rho R^3}{\sigma} \right)^{1/2} \tag{33}$$

which results (due to parameters presented in Table 1) in factor of 5 between the two simulations presented in Fig. 7, accounted for in the figure. Unlike the high-We regime, in which expansion is rapid and nearly uniform, the low-We regime exhibits higher variance in pore volumes, with a number of implosion events visible towards the end of recorded time. This proves that the presented numerical method is capable of capturing the transition between the two regimes, provided that simulation covers a sufficient temporal range[5].

5.3. *Evolution of the pressure field*

We continue our comparison of the presented uniaxial expansion regimes with Figs 8a and 8b, first of which displays the evolution of averaged pressure field

$$\langle p \rangle = \frac{1}{V} \int_V p dV \tag{34}$$

for both analyzed flow regimes. As the high-We regime is characterized by a more violent decrease in average pressure in the initial parts of expansion, it was necessary to plot $\langle p \rangle$ in logarithmic scale in Fig. 8a. However due to the function being negative, we instead plot in Fig. 8a the

$$\log(|\langle p \rangle|) \cdot \mathrm{sgn}(\langle p \rangle). \tag{35}$$

It is clearly visible that the rapid decrease from $e^{10} \approx 2.2 \cdot 10^5$ to zero is followed by a period for which $\langle t \rangle < 0$.

Figure 8b presents a plot comparable to Fig. 8a but obtained by discarding Laplace pressures (i.e. capillary contributions). Here, we are using only input from grid cells that do not coincide with pore surfaces (this can be found from values of C function)—in other words, grid-cells away from the pores and the interface. This can be roughly approximated by

$$\langle p \rangle = \frac{1}{V} \int_V p(1 - C) dV \tag{36}$$

where C stands for the fraction function. Accuracy provided by (36) is moderate as it will still include contributions from direct neighbours of the interface grid-cells; those neighbouring cells are generally still influenced by Laplace pressures. While better accuracy could be provided by a distance function-based methods (Aniszewski et al., 2014), above formula is enough to yield a much different result than depicted in Fig. 8a. Indeed, while a similar pressure evolution as in Fig. 8a is observed in Fig. 8b, we notice that

$$\forall t \colon \left\{ \langle p \rangle(t) > 0 \ \wedge \ \frac{\partial \langle p \rangle}{\partial t} < 0 \right\}, \tag{37}$$

which is to say average pressure is always positive and decreasing. Additionally, slight oscillations visible in Fig. 8a for $0.025 < t < 0.035$ are not found in Fig. 8b, thereby reassuring us that they were attributed to the capillary forces.

A different $\langle p \rangle$ evolution is observed for the "competition" regime. In Fig. 9 for low We, which (as we mentioned in context of Fig. 4) is dominated by capillary pressures nearly from the onset, we notice $\langle p \rangle \in [-50, -20]$ within the computed time interval. For $t > 0.15$ individual peaks are visible (as triangles in Fig. 9) which should be associated with implosion (collapse) events. It is easy to note that unlike the isolation regime, in the competition regime we find for $t > 0.02$

$$\frac{\partial \langle p \rangle}{\partial t} > 0, \tag{38}$$

i.e. average pressure is steadily growing, which in fact is predicted by (19). We would associate this with the initially rapid expansion slowing down, and competition process taking over.

[5] Which in turns depends directly on numerical grid resolution. The smaller $R(t_1)$ the more timespan will be included in the simulation before the pores coalesce.

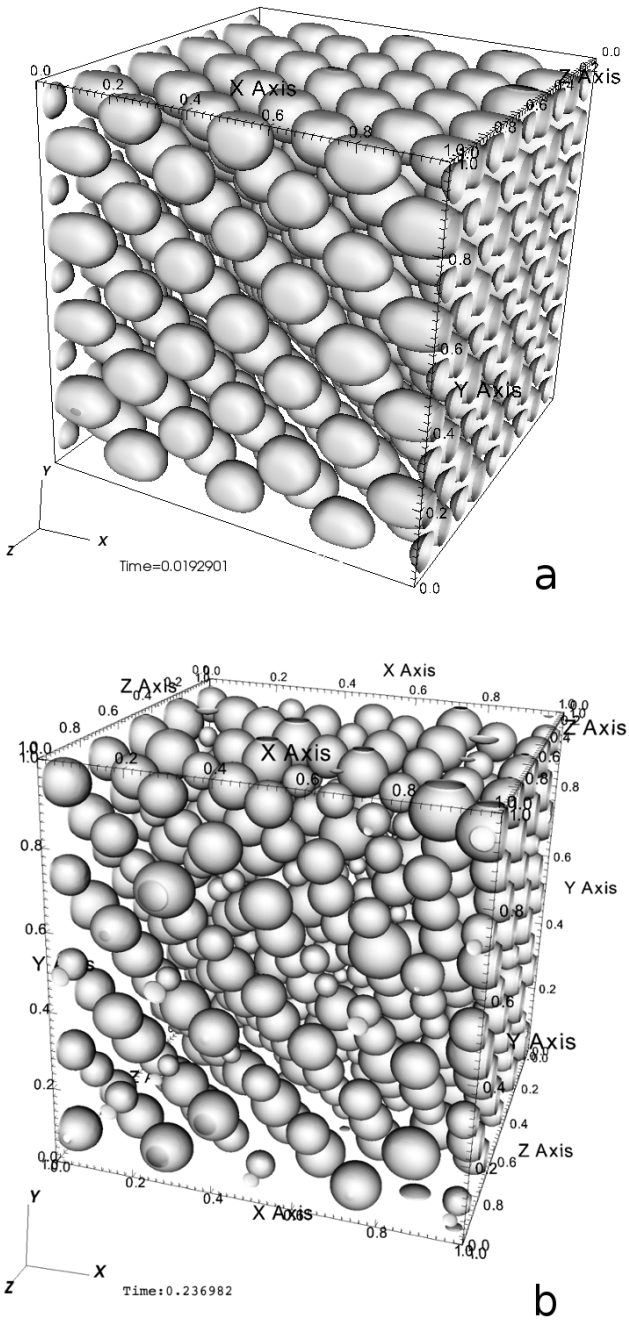

Figure 4: (a) Simulation of the flow characterized by We = 512. (isolation regime) at $t = t_1 + 1.92 \cdot 10^{-2}$. (b) Simulation of the pore lattice at We = $3.3 \cdot 10^{-2}$ ("competition" regime) for $t = t_1 + 0.237$.

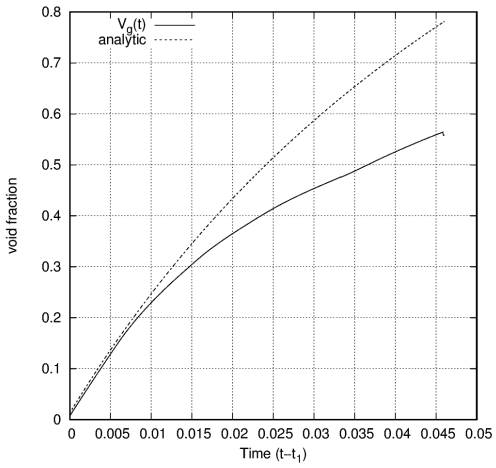

Figure 5: Volume fraction temporal evolution. Continuous line: simulation; dashed line: using (32).

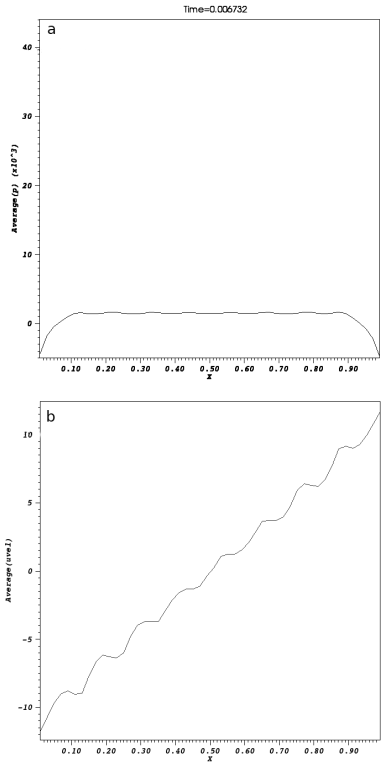

Figure 6: Isolation regime: Averaged (in YZ) profiles of u and p for $t - t_0 \approx 6 \cdot 10^{-3}$.

The first expansion phase (or the isolation regime) corresponded to rapid expansion when the pores are still small compared to ℓ, while the latter is due to Laplace (capillary) pressures which—in spite of being inversely proportional to pore radii—become dominant, and competition phenomenon appears (Malan et al., 2018). Note that measured in absolute time values, evolution presented in Fig. 9 involves a temporal interval nearly ten times longer than that of Fig. 8.

To further validate the predictions of the numerical simulation result presented in Figure 9 we have included a curve displaying temporal evolution of $p_\infty(t)$ calculated using (19). The sharp pressure drop resulting from initial shock as well as the beginning of pressure growth after minimum is reached (mentioned in Section 2) are well visible in Fig. 9 for both curves, and there is overall agreement in their shape. Obviously, mean pressure $\langle p \rangle$ is not equal to p_∞ and is strongly influenced by the capillary pressures originating from surface tension on pore surfaces. For this reason, minimum p value is predicted too low. Interestingly, if instead of using $\sigma = 1$ in (19) we calculated p_∞ using $\sigma = 1.3$, we get $\min_t(p_\infty(t)) = \min_t(\langle p \rangle(t))$

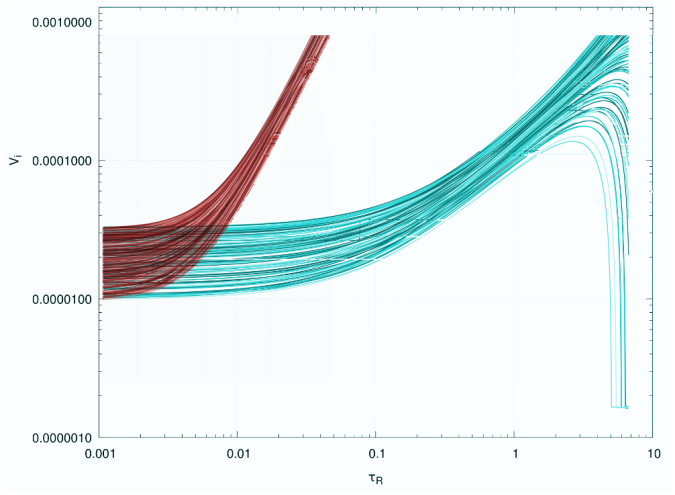

Figure 7: Pores volume history for We = 512 (brown), and We = 0.03 (blue) flows.

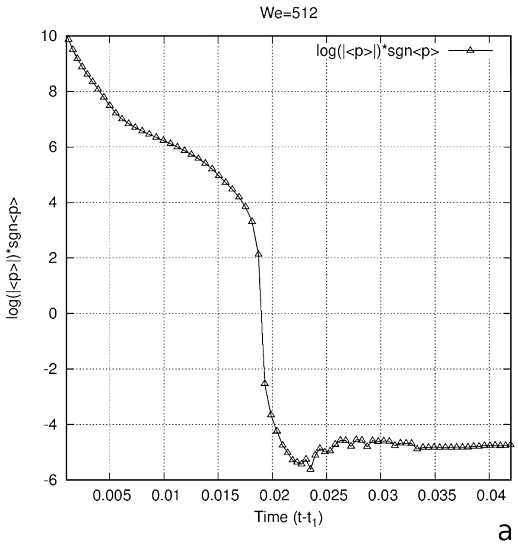

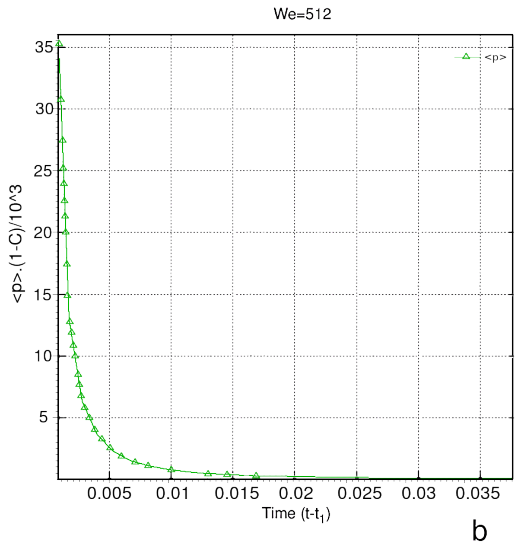

Figure 8: Isolation regime: (a) Evolution of the domain-averaged pressure for the flow at We = 512; (b) The same quantity prepared by including only grid cells in the liquid.

and a better agreement of the p_∞ curve to $\langle p \rangle$ overall which strongly suggests that indeed the contributions of Laplace pressures substitute the difference between the analytic prediction and simulation result.

Figure 10 presents an example of an additional simulation[6] with $\mathrm{We}(t) = 9.56 \cdot 10^{-2}$ at $t = t_0 + 0.157$. This third presented simulation corresponds to a transition from isolating to competing regimes predicted by (15a). We can illustrate this by directing our attention to values of pressure inside the pore cluster. In Fig. 10, three isosurfaces are presented. First, a gray (semi-transparent) isosurface of fraction function C is visible. This marks the position of individual pores, although at first glance it is hard to conclude if the competition phenomenon is present. Similarly, regions with $p \approx -42$ (green, semi-transparent isosurface in Fig. 10) exhibit little spatial variability: all pores are surrounded by them. However, once an isosurface for $p \approx -63$ is drawn (solid blue surface in Fig. 10) we notice that homogeneity is no more: pressure attains this value only close to certain pore's surface. Upon closer inspection it is evident these pores have smaller radii (hence larger mean curvatures); they are being acted upon by other, growing pores to eventually succumb to the competition (Malan et al., 2018).

6. Conclusions

We have presented a numerical simulation setup that permits prediction of the behavior of a pore lattice within rapidly expanding medium.The expansion corresponds to a uniaxial (one-dimensional) ballistic phenomenon characterized by large initial outward velocity magnitudes which then immediately diminish. On one hand, this setup facilitates recognition of momentum-dominated phenomena such as rapid pore elongation in "isolation" regime. On the other, the decline in expansion rate promotes the onset of pore "competition" and more anisotropic radii distribution in surviving pores. Moreover, simulations allow us to observe transition between these two regimes. We have presented that instantaneous velocity and pressure profiles match analytic predictions, and so does the temporal pressure evolution in the simulated pore systems.

It is relatively easy to point out numerous simplifications of the presented model. One example is the lack of solution inside pore interiors, another is using an incompressible medium. Still the work presented provides us with insights into the micro-spall process which is otherwise inaccessible experimentally: simulation domains here correspond to micrometers while temporal span is of similar order, forcing physicists and engineers to indirect analysis. In this context the present study—especially with its choice of (partly periodic) boundary conditions—may easily be used as a departure point for larger-scale modeling e.g. in the context of metal breakup under load.

[6]The simulation uses the same boundary conditions as those mentioned above, resolution is 512^3 grid points.

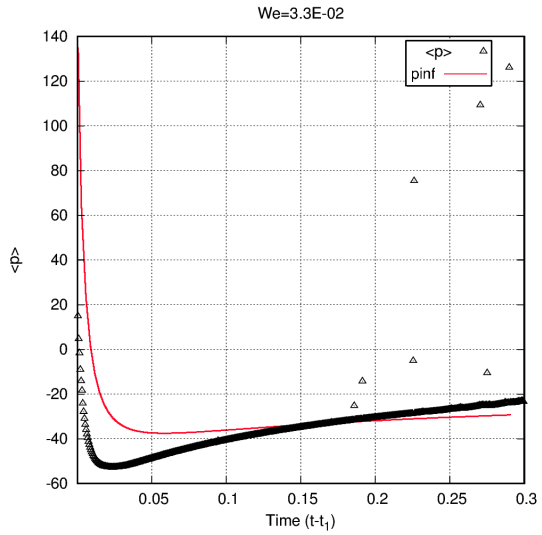

Figure 9: Evolution of the mean pressure field for the competition regime. Numerical simulation (black triangles) and analytical $p_\infty(t)$ using (19) (red line).

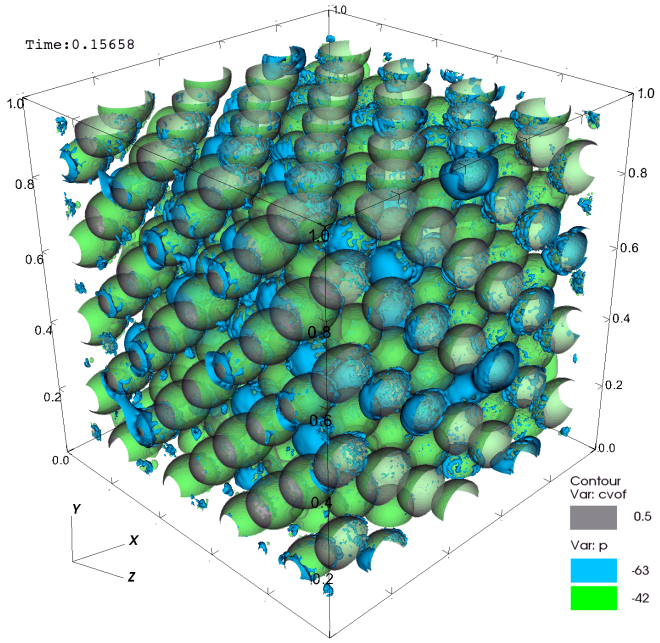

Figure 10: The bubble cluster at We $\approx$ 0.1, corresponding to a transition from isolation to competition regime.

References

Aniszewski, W., Ménard, T., Marek, M., 2014. Volume of Fluid (VOF) type advection methods in two-phase flow: A comparative study. Comput. Fluids 97 (0), 52–73.

Batchelor, G., 1967. An introduction to fluid dynamics. Cambridge University Press.

Caflisch, R., Miksis, M., Papanicolaou, G., Ting, L., 1985. Effective equations for wave propagation in bubbly liquids. J. Fluid Mech. 153, 259–273.

Cummins, S., Francois, M., Kothe, D., 2004. Estimating curvature from volume fractions. Comput. Struct. 83 (6–7), 425–434.

de Rességuier, T., Signor, L., Dragon, A., Roy, G., 2010. Dynamic fragmentation of laser shock-melted tin: experiment and modelling. Int. J. Fracture 163 (1–2), 109–119.

Everitt, S., Harlen, O., Wilson, H., 2006. Competition and interaction of polydisperse bubbles in polymer foams. J. Non-Newt. Fluid 137 (1–3), 60–71.

Falgout, R., Yang, U., 2002. hypre: a library of high performance preconditioners. In: Sloot, P., Hoekstra, A., Tan, C., Dongara, J. (Eds.), Computational Science – ICCS 2002. Vol. 2331 of Lect. Notes Comput. Sc. Springer, pp. 632–641.

Girifalco, L. A., 2000. Statistical Mechanics of Solids. Oxford University Press, New York.

Hirth, C., Nichols, B., 1981. Volume of Fluid (VOF) method for the dynamics of free boundaries. J. Comput. Phys. 39 (1), 201–225.

Ilinskii, Y., Hamilton, M., Zabolotskaya, E., 2007. Bubble interaction dynamics in Lagrangian and Hamiltonian mechanics. J. Acoust. Soc. Am. 121 (2), 786–795.

Li, J., 1995. Calcul d'interface affine par morceaux. C.R. Acad. Sci. II B 320 (8), 391–396.

Ling, Y., Zaleski, S., Scardovelli, R., 2015. Multiscale simulation of atomization with small droplets represented by a Lagrangian point-particle model. Int. J. Multiphas. Flow 76, 122–143.

Malan, L., Ling, Y., Scardovelli, R., Llor, A., Zaleski, S., 2018. Direct numerical simulations of pore competition in idealized micro-spall using the VOF method. Comput. Fluids (submitted) also available as arXiv:1711.04561 [physics.flu-dyn].

Malan, L., Zaleski, S., 2015. Numerical simulation of bubble competition during micro-spalling. Tech. Rep. 13-39-C-DSPG/CAJ, Institut Jean le Rond d'Alembert.

Popinet, S., 2003. Gerris: a tree-based adaptive solver for the incompressible Euler equations in complex geometries. J. Comput. Phys. 190 (2), 572–600.

Scardovelli, R., Zaleski, S., 2000. Analytical relations connecting linear interfaces and volume fractions in rectangular grids. J. Comput. Phys. 164 (1), 228–237.

Shu, C.-W., 1997. Essentially Non-Oscillatory and Weighted Essentially Non-Oscillatory schemes for hyperbolic conservation laws. Tech. Rep. CR-97-206253, NASA.

Signor, L., de Rességuier, T., Dragon, A., Roy, G., Fanget, A., Faessel, M., 2010. Investigation of fragments size resulting from dynamic fragmentation in melted state of laser shock-loaded tin. Int. J. of Impact Eng. 37 (8), 887–900.

Sweby, P., 1984. High resolution schemes using flux limiters for hyperbolic conservation laws. SIAM J. Numer. Anal. 21 (5), 995–1011.

Tryggvason, G., Scardovelli, R., Zaleski, S., 2011. Direct numerical simulations of gas–liquid multiphase flows. Cambridge University Press.

Youngs, D., 1984. Numerical simulation of turbulent mixing by Rayleigh–Taylor instability. Fronts, Interfaces and Patterns, 32.